PNAS

Main Manuscript for

Kinetic Control over Disproportionation Stabilizes Wurster's Blue as Persistent Catholyte Redoxmer for Nonaqueous Redox Flow Batteries

Xiaoting Fang,[a,b,c,§] Zhiguang Li,[a,b,c§] Lifan Zeng,[d] Diqing Yue,[c] Lily A. Robertson,[b] Yuyue Zhao,[b,c] Ilya A. Shkrob,[a,b] Xiaoliang Wei,[c,*] Lu Zhang,[a,b,*]

[a] Joint Center for Energy Storage Research, Argonne National Laboratory, Lemont, IL 60439, United States

[b] Chemical Sciences and Engineering Division, Argonne National Laboratory, 9700 South Cass Avenue, Lemont, IL 60439, United States

[c] School of Mechanical Engineering, Purdue University, 585 Purdue Mall, West Lafayette, IN 47907, United States

[d] Chemical Genomics Core, School of Medicine, Indiana University, 410 West 10th Street, Indianapolis, IN 46202, United States

* Xiaoliang Wei: wei304@purdue.edu

* Lu Zhang: zhanglu77@gmail.com

Author Contributions: X.W. and L.Z. designed the research; X.F., Z.L. and I.A.S. performed the research; L.Z.,D.Y., S.B., L.A.R., Y.Z., and I.A.S. contributed new reagents and analytic tools; I.A.S., X.W., and L.Z. analyzed data; X.F., Z.L., I.A.S., X.W., and L.Z. wrote the paper.

Competing Interest Statement: The authors declare no competing interest.

Classification: Physical Sciences

Keywords: nonaqueous redox flow battery, organic, stability, disproportionation, kinetic control

This PDF file includes:

Main Text
Figures 1 to 4

Abstract

Organic redox molecules, or redoxmers, are attractive as lower cost materials for nonaqueous redox flow batteries; however, insufficient stability of their charged states remains a challenge. A

common reaction of these redoxmers is charge transfer equilibria that yield unstable multiply charged states, shifting the overall reaction towards the decomposition products. Here we show how kinetic controls can be engineered into a redoxmer molecule to suppress these unwanted reactions by providing steric hindrance and slowing down the decay of the multiply charged intermediates. This approach was used to transform Wurster's Blue, which is historically the first example of a radical ion in organic chemistry, into an exceptionally stable species that persists over thousands of electrochemical cycles. Our strategy suggests a new pathway to stabilization of organic redoxmers, which is essential to achieving high energy density and long cycle life.

Significance Statement

Paste your significance statement here. Please note that it should not exceed 120 words, but should be at least 50 words in length. It should not include any references.

Main Text

Introduction

Using intermittent sources of power such as solar and wind requires large-scale energy storage to solve the challenge of intermittency. Redox flow batteries (RFBs) provide a promising approach to grid energy storage, in which energy-bearing redox materials (i.e., redoxmers) are dissolved in liquid electrolytes that are stored in external reservoirs and are pumped through electrodes during electrochemical cycling. This design leads to independent control over energy and power with a potential for flexible scaling up. Over the last decade, there was rapid progress in the development and commercialization of aqueous RFBs.[1, 2] Among them, vanadium RFBs are the most advanced systems, but the market penetration is hindered by high materials cost and limited energy density (25~30 Wh L^{-1}). Nonaqueous RFBs (NRFBs) present an attractive alternative by offering wider electrochemical stability windows (up to 5 V, compared to <1.5 V for aqueous systems) and more choices of redoxmers, potentially leading to energy-dense, cost-effective storage systems.[3, 4] Organic redoxmers have gained momentum for NRFBs due to their structural diversity, molecular tailorability, and lower cost.[5-7] However, significant gaps still exist as the current organic redoxmers are unable to satisfy the strict requirements for commercially competitive NRFBs.

Among these requirements, extremely high (by the standards of organic chemistry) chemical and electrochemical stability of their charged states remains the greatest concern as it determines the cycle life and calendar life of the flow cell. Charging of organic molecules yields chemically reactive states whose compatibility with electrolyte needs to be carefully assessed.[8] Furthermore, these species may undergo cross reactions with each other and/or progenitor molecules causing irreversible loss of capacity during electrochemical cycling and charge storage.[9-11] A particularly vexing parasitic reaction limiting redoxmer ~~lifetime~~stability, especially at high concentrations, occurs when a redoxmer has more than one charged state involved in charge transfer equilibria. Due to such reactions, the unstable multiply charged states can be accessed even when the electrode potential is adjusted so that only singly charged molecules are generated at the electrode. The disproportionation of two singly charged molecules to a neutral progenitor and a doubly charged molecule is the common occurrence of such equilibria.

While thermodynamically the charge transfer equilibrium favors the more stable states, irreversible decomposition of the less stable multiply charged states shifts it towards the decomposition products, resulting in the overall decay of charge carriers in solution. This reaction accelerates when the concentration of the redoxmer is increased or the redoxmers are clustered together as pendant groups in macromolecular scaffolds that are used to block membrane crossover.[12] A general strategy for suppressing these unwanted reactions is needed to achieve

higher energy densities and longer cycle lives. Since the energetics of the charge transfer equilibria is "fixed" by the redox potentials that cannot be widely tuned, thermodynamics alone cannot suppress these parasitic reactions, so kinetic controls need to be engineered to slow them down.

Here we report a molecular design strategy to improve the stability of organic catholyte molecules (positive charge carriers) through suppression of disproportionation of their radical cations (singly charged states). Historically, Wurster's blue, which is the trivial name for the oxidized *N*,*N*,*N'*,*N'*-tetramethyl-*p*-phenylenediamine (TMPD), was the first example of a radical ion identified by the great Leonor Michaelis.[13] TMPD derivatives have been evaluated in energy storage, e.g., as redox mediators in flow batteries and lithium air batteries.[14, 15] While TMPD can be useful in these applications, its use as a redoxmer in electrolytes is limited by the tendency of $TMPD^{+\bullet}$ to undergo disproportionation that yields the unstable dication ($TMPD^{2+}$, see below). This reaction occurs both in solution[16, 17] and in solid $TMPD^{+\bullet}$,[18, 19] where it is facilitated by overlapping π-orbitals in the planar radical cations.[20-23] Aiming to suppress these unwanted reactions, we reasoned that crowding of radical cations with bulky groups can prevent their close face-to-face approach, reducing the rate of the forward charge transfer. Synthetically, this steric protection was achieved by introducing phenyl and oligo(ethylene glycol) ether substituents in the diamino groups. In symmetric flow cells, some of these sterically protected TMPD derivatives exhibit exceptional performance, resulting in 7,300 cycles with an overall capacity fade of 6% over 90 days.

Results

Attracted by the high solubility of TMPD in polar organic solvents (3.2 M in acetonitrile, MeCN), we first studied this progenitor molecule, but discovered that it was unsuitable for NRFBs. To demonstrate that, electron paramagnetic resonance (EPR) was used to characterize the decay kinetics of 50 mM $TMPD^{+\bullet}$ in an electrolyte consisting of 0.5 M lithium bis(trifluoromethanesulfonyl)imide (LiTFSI) in MeCN. The first-derivative EPR spectra (Figure 1a) were doubly integrated to obtain the EPR signal as a function of time. This quantity is proportional to the number of unpaired electrons in solution, and its decrease over time reflects the delayed decomposition of $TMPD^{+\bullet}$ to diamagnetic products. The obtained half-life time ($t_{1/2}$) of 16.5 h is too short for practical use. Replacing Li^+ ion with organic cation *N*-methyl-*N*-butylpyrrolidinium ($PYR14^+$, to make possible significant increases of the redoxmer and salt concentrations, e.g., to 25 mol%) resulted in even shorter lifetime of 12 h (Figure S1a). This time further reduced to < 1 h when the concentration of $TMPD^{+\bullet}$ increased to 25 mol% (Figure S1b), as can be expected for a disproportionation reaction. A series of liquid chromatography – mass spectrometry (LC-MS) and nuclear magnetic resonance (NMR) studies were carried out to chemically prepared $TMPD^{+\bullet}$ to elucidate its decomposition mechanisms (Sections S1-S2, Figures S2-S4). LC-MS detected the existence of proton (H^+) and *N*-methyl (Me^+) loss products in aged $TMPD^{+\bullet}$ solutions. A beige-colored polymeric product was obtained, and the structure indicates the presence of a cationic backbone with PF_6^- anions as well as the bis-methylated phenylenediamine rings bridged through methylene carbons. These analyses demonstrate a disproportionation-based decomposition pathway shown in Scheme S1. The dication of TMPD ($TMPD^{2+}$) is not stable and undergoes facile deprotonation and *N*-demethylation reactions that shifts the charge transfer equilibrium indirectly causing rapid decay of the radical cation. From these observations, we hypothesized that substitution of TMPD at the nitrogen with bulky groups, including the *N*-phenyl groups that could not be easily eliminated from the dication, can both inhibit the disproportionation and improve the stability of dication, so the overall reaction becomes shifted towards the radical cation. Since substitution of such bulky groups can decrease solubility of the redoxmer, ether chains were introduced into the amino groups to restore it.[24] Each modification was followed by a lifetime measurement using EPR spectroscopy to guide the design towards the most stable and soluble molecules.

Figure 1b illustrates the molecular design trajectory. First, TMPD was modified, separately, with the phenyl and 2'-methoxyethyl groups to afford *N*,*N'*-dimethyl-*N*,*N'*-diphenylbenzene-1,4-diamine (MDPD) and *N*,*N'*-bis(2'-methoxyethyl)-*N*,*N'*-dimethylbenzene-1,4-diamine (MEMBD), respectively. Based on both our calculations (see below) and EPR measurements (Figure S5), the *N*-phenyl ring protons have small hyperfine coupling constants (hfcc's) indicative of minimal pi-conjugation over the radical cation, so these groups primarily serve as steric protection groups.

As indicated by the EPR kinetics (Figures 1c and S6), $MDPD^{+\bullet}$ shows >10X improved chemical stability vs. $TMPD^{+\bullet}$ with a $t_{1/2}$ of 230 h, suggesting that, even with the *N*-methyl groups retained, the introduction of *N*-phenyl groups considerably improves the stability of radical cation. However, as these are bulky and solvent-phobic groups, MDPD exhibits low solubility of just 3.2 mM in MeCN. In contrast, the ether derivatized MEMBD is liquid at 25 °C and fully miscible with the solvent. Interestingly, $MEMBD^{+\bullet}$ also exhibits improved chemical stability ($t_{1/2}$ = 162 h) compared to $TMPD^{+\bullet}$, suggesting that crowding of the amino group in general improves the stability.

In the next iteration, we combined the ether chains *and N*-phenyl groups in MEDPD, obtaining yet another tenfold increase in the lifetime $t_{1/2}$ of 2,295 h (95 d). While such persistence would make MEDPD a good candidate for use in NRFBs, the solubility of this molecule was only 0.37 M in MeCN. In the final iteration, a longer ether chain was introduced to obtain *N,N'*-bis(2'-(2"-methoxyethoxy)ethyl)-*N,N'*-diphenylbenzene-1,4-diamine (MEEDPD). Like MEMBD, it is also liquid and readily miscible with MeCN, but unlike $MEMBD^{+\bullet}$, $MEEDPD^{+\bullet}$ was extremely stable, with $t_{1/2}$ of 3,882 h (162 d). This is one of the longest lifetimes recorded for a radical cation in solution, proving the viability of our approach. Equally importantly, all four TMPD derivatives were prepared using one-step synthesis from inexpensive chemicals, suggesting an advantage of cost-effectiveness.

To better elucidate the mechanism for the observed stability, density functional theory (DFT) calculations were performed to determine the optimized molecular geometries and energetics of these redoxmers in different states of charge. These geometries are shown in Figure 2. In neutral TMPD, the two amino groups are puckered, while the charged molecule becomes planar and highly symmetric (D_{2h}). Linus Pauling was the first to connect this symmetry and the exceptional stability of $TMPD^{+\bullet}$, reasoning that side reactions would break this symmetry, leading to higher reaction barriers.[] With the *N*-substitution in the amino groups, both the neutral molecules and their charged states are no longer planar due to steric strain introduced by these bulky groups. The strain causes these groups to rotate out of the plane of phenylenediamine ring. The dihedral angles between the latter and the *N*-phenyl ring in neutral MDPD, MEDPD, and MEEDPD are 70-82° changing to 70-72° in their charged states (Table S1 in Section S3). Likewise, for the *N*-ether groups, the corresponding dihedral angles are 45-56° in the neutral states and 25-40° in the charged states. These propeller-like conformations make such groups efficient steric protectors, explaining their ability to suppress disproportionation.

There is another interesting structural property of these molecules that is less obvious: as the two amines are identically substituted, the molecule can be either mirror- or centro- symmetric (the C_2 and C_i states, respectively). In the neutral and singly charged MEMBD and MDPD, these two conformers are almost degenerate in energy, so the molecules can flex between the two conformations. In contrast, MEDPD and MEEDPD are conformationally locked in the mirror symmetry in all states of charge. While there is the usual chain dynamics in the ether groups, the *bis*-*N*-phenyl-phenylenediamine core of these molecules is "frozen". This property makes the charged states more rigid and less prone to the symmetry-preserving reactions like the loss of *N*-alkyl groups, recapitulating Pauling's rationale for the exceptional stability of $TMPD^{+\bullet}$. A good correspondence of magnetic parameters computed for symmetric $MEDPD^{+\bullet}$ and $MEEDPD^{+\bullet}$ with the ones obtained for EPR spectroscopy (Figure S5) strongly supports the high symmetry of these radical cations, validating our structural insights.

While the exceptional stability of electrochemically generated charged species is obviously necessary for long-term charge storage in extant reservoirs, equally important is the cycling stability. These two metrics do not always correlate as there are parasitic reactions that occur only near the electrodes. The electrochemical behaviors of the TMPD derivatives were first investigated using cyclic voltammetry (CV). Both $1e^-$ and $2e^-$ oxidation is observed (Figure S7 and Table S2), corresponding to the formation of a radical cation and a dication, respectively. On the time scale of the CV scans, these electrochemical reactions are reversible, with the exception of $2e^-$ oxidation of MDPD. The large energy gap between the $1e^-$ and $2e^-$ redox reactions (>0.5 V for all molecules) explains why the charge transfer equilibrium in the solvent bulk is strongly shifted towards the radical cation. Figure 3 compares cyclic voltammograms for one-electron oxidation of 5 mM redoxmer in 0.5 M LiTFSI/MeCN at a sweep rate of 100 mV s^{-1}. TMPD has a redox potential of -0.206 V vs Ag/Ag^+. Substituting the *N*-methyl with ether chains in MEMBD does not change the redox potential appreciably, but incorporating the *N*-phenyl groups increases it by over 0.25 V. As shown in Figure S8, the experimental $1e^-$ and $2e^-$ redox potentials linearly correlate with the number of heteroatoms in the substituent groups and the presence of the *N*-phenyl groups. For the $2e^-$ oxidation, this trend is reproduced in our DFT calculations, but for $1e^-$ oxidation the correspondence is less exact, although the more positive potential for *N*-phenyl derivatives is reproduced in these calculations, too.

The CVs at different scan rates were obtained to estimate the diffusion coefficients by the Randles–Sevick analysis in Table 1 (Figures S9-S13).[25] TMPD shows the highest diffusivity of 12.7×10^{-6} cm^2 s^{-1} while the bulkier derivatives are slower, as can be expected form their relative size. The electron transfer rate constants for the redoxmers were calculated using the Nicholson's method[26] and found to be $\approx10^{-2}$ cm s^{-1} for all molecules.

As the charged MEEDPD has the longest lifetime, it was selected for further electrochemical experiments. Due to the lack of selective membranes for NRFBs, assessing the cycling stability of molecular redoxmers has been a challenge as it is always compromised by migration of the small molecules across the membrane. In this regard, symmetric flow cells, where the same molecule in different states of charge is present in both cell compartments, have been used to minimize such interference.[27, 28] In our test, a symmetric cell with a Daramic porous separator (Figure 4a) was used. MEEPD was electrochemically charged to 50% theoretical capacity using bulk electrolysis (Figure S14) and then introduced to both compartments of a symmetric flow cell.

Figure 4b-c show the time profiles for voltage and capacity for a symmetric flow cell galvanostatically cycled at different current densities, with the cycles interrupted at attainment of set voltages. An area-specific resistance of 9.4 Ω cm^2 was measured for this cell using electrochemical impedance spectroscopy (EIS, Figure S15). As the current density increases from 20 to 50 $mAcm^{-2}$, the cell polarization increases and the material utilization decreases from 85% to 69%. The long-term cycling is illustrated in Figure 4d. At a current density of 50 mA cm^{-2}, each cycle took ≈18 min. High coulombic efficiency (CE) was maintained over 7,300 cycles with the mean value of 99.7%. During the cycling, volume losses were observed due to slow evaporation of MeCN through the seals around the membrane. This loss causes increased resistance through greater association of electrolyte ions, so periodically a fixed volume of the solvent was added to each cell compartment, which is denoted as event "A" in Figure 4d. In addition, we periodically rebalanced the electrolyte by mixing the solutions from the two compartment and then dividing them equally between them (denoted as "R").[29] The nearly identical voltage profiles after each such step (Figure S16) suggests the effectiveness of this procedure (which is also practiced for vanadium aqueous flow cells). With this periodic maintenance, capacity retention of 94% was obtained after 90 days, corresponding to an average rate for capacity fade of 0.067% per day of cycling.

The symmetric flow cell was then evaluated at a higher redoxmer concentration (Figure S17) that is more typical of practical applications. We remind that the rate of disproportionation increases

with the concentration of charge carriers in electrolyte, so this test is essential in demonstration that our design strategy has addressed the problem. Figures 4e shows capacity fade and CE profiles for a 0.5 M MEEDPD symmetric flow cell operated at a current density of 50 mA cm^{-2}. Due to a higher concentration of electrolyte, solvent evaporation caused still more capacity loss due to a steeper decrease in ionic conductivity caused by the solvent removal from electrolyte. To compensate, a fixed volume of the solvent (12 mL) was added to each cell compartment every 8 days. Each such solvent addition restored the lost capacity almost to the initial level (Figure S18). The 0.5 M symmetric flow cell showed stable cycling over 500 cycles with an overall capacity retention of 92.5% over 32.5 days. With the periodic solvent replacements, the cell resistance slowly increased by 30% over this period of time (Figure S19).

Such stable cycling at high concentration implies that the disproportionation reactions have been largely suppressed in this redox system, and the cycling lifetime is limited by the imperfect cell design. Also worth mentioning is that cycling of MEEDPD is impervious to air leaks that are difficult to avoid in a commercial setting. To show that, a symmetric H-cell containing 2 mM MEEDPD was operated *in air*, yielding the average CE of 99.1% over 200 cycles (Figure S20). Such oxygen resistance is rarely seen for radical ions.

In full cells, the cycling of redoxmers is affected by crossover between the cell compartments: the redox active molecules and products of their decomposition eventually migrate across the membrane, causing parasitic reactions. Given the ~~relatively low~~mild redox potential of TMPD derivatives, to obtain cell voltage > 1 V, ~~these catholytes needs to be paired with~~ low-potential anolytes such as 2,1,3-benzothiadiazole (BzNSN) are required, whose charged states are highly reactive organic bases.[10, 30] As shown in Figure S21, a MEEDPD/BzNSN flow cell using mixed electrolytes in both cell compartments exhibits a continuous capacity loss over 160 cycles, which is a fraction of the cycle lifetime observed for MEEDPD in symmetric cells. Given the dearth of suitable low potential, yet stable anolytes, we were unable to pair MEEDPD with an anolyte that would showcase its exceptional stability while yielding voltages > 1V, which is a reflection on the exceptional electrochemical stability of MEEDPD.

Discussion

To conclude, we have demonstrated how an organic catholyte can be stabilized through the suppression of charge transfer equilibria shifted towards the by-products due to involvement of unstable multiply charged states. These reactions are a hurdle to achieving high energy densities in all redoxmer systems. Since the free energy of charge equilibria cannot be widely tuned, only kinetic control are possible. We demonstrate how to achieve this control by (i) engineering steric hindrance preventing close approach between the charged molecules, (ii) slowing down the decomposition of a multiply charged states by strengthening bonds between the redox core and the bulky groups, and (iii) using molecules that are conformationally locked in their symmetric states in all states of charge. A combination of these three approaches allowed us to transform a relatively unstable radical cation (Wurster's blue) to one of the most stable organic catholytes identified so far, to the extent that we cannot find a stable low-potential anolyte to pair it with in full cells. Two more properties were engineered into this molecule, one intentionally (solubility), another indvertantly (oxygen resistance). To obtain higher solubility, ether chains were used to obtain a liquid catholyte that is miscible with electrolyte. Our molecular design shows how beneficial traits can be combined in a small redox active molecule to obtain exceptional performance. It also suggests that unexpected and practically interesting properties can occur in such molecules that are not part of the planning.

Finally, we note that charge equilibria often prevent the use of redox-active molecules as pendant groups in oligomer and polymer scaffolds, where these charged groups can be close to each other, accelerating their decay. While this tendency can be addressed by making rigid scaffolds preventing the encounters, such scaffolds often suffer from low solubility and synthetic

complexity. As these macromolecular scaffolds can be used with size-selective nanoporous membranes to block the crossover, overcoming this common hurdle is pivotal for further evolution of the "redoxmer" concept that presently offers the only viable solution to the crossover in the NRFBs.

Experimental

CV Measurement. CV was performed at 25 °C in a three-electrode cell using a CHI760D potentiostat (CH Instruments) with *iR* compensation. A glassy carbon electrode (3 mm diameter) served as a working electrode, while an $Ag/AgNO_3$ electrode (10 mM in MeCN) and a platinum wire were used as the quasi-reference and counter electrodes, respectively. The electrolyte contained 5 mM redoxmer (TMPD, MEMBD, MEDPD or MEEDPD) or 2 mM MDPD in 0.5 M LiTFSI/MeCN. Unless specified otherwise, the voltammograms were collected at a scan rate of 0.1 V s^{-1}. The CV curves were obtained at the scan rates u varying from 0.01 to 0.5 V s^{-1} to determine the diffusion coefficient (D) using the Randles-Sevcik Eq. (1)[25]:

$$i_p = 0.4463\,(nF)^{3/2}AC(uD/RT)^{1/2} \quad (1)$$

where i_p is the peak anodic or cathodic current (in A), n is the number of transferred electrons, F is Faraday constant (96,485 C mol^{-1}), A is the electrode area (0.071 cm^2), C is the redoxmer concentration in the solution bulk (in mol cm^{-3}), T is the temperature (in K), and R is the gas constant (8.314 J K^{-1} mol^{-1}). The diffusion coefficients D were estimated from the slopes of the i_p vs. $u^{1/2}$ curves. The electron transfer rate constant (k_0) was estimated using the Nicholson's method from Eqs. 2 and 3:

$$\Psi = (-0.6288 + 0.0021\Delta E_p)/(1 - 0.017\Delta E_p) \quad (2)$$

$$\Psi = k_0(\pi DnF/RT)^{-1/2}u^{-1/2} \quad (3)$$

where Ψ is the kinetic parameter, ΔE_p is the peak separation in the voltammogram, and D is the average diffusion coefficient from Eq. 1. The rate constant k_0 was calculated from the slope of the Ψ plotted vs. $u^{-1/2}$ (Figures S9-S13).

EPR Analysis. The H-type bulk electrolysis cell according to a reported design[31] was used to generate charged radical cations for EPR analysis, using constant current charging to a set potential or set capacity. The charged solution was placed in a glass capillary and contained in a Pyrex glass tube with a piston seal (Wilmad-Lab Glass model 734-LPV-7). Continuous wave EPR spectroscopy was used to observe radicals *in situ* and study their decay kinetics. The first-derivative EPR spectra were obtained at 25 °C using a Bruker ESP300E X-band spectrometer operating at ~9.44 GHz with 100 kHz field modulation at 0.2 G (1 G = 10^{-4} T). The EPR spectra obtained at >5 mM redoxmer were broadened to a singlet line due to rapid spin exchange in solution, so dilution was needed to resolve these EPR spectra. Analyses of the resolved EPR spectra was carried out using WinSim program suite publicly available at https://www.niehs.nih.gov/research/resources/software/tox-pharm/tools/index.cfm. For kinetic analyses, the EPR spectra were recorded at the constant time intervals, centered, background corrected, and doubly integrated.

DFT Computation. DFT calculations were performed using the Gaussian 16 suite[32] and the 3-parameter hybrid Becke 88 exchange functional with Lee-Yang-Parr correlation functional (B3LYP) and 6-311++G(d,p) basis set. The MeCN solvent was simulated using the polarizable continuum model.[33, 34] Geometry optimization and vibration frequency calculations were performed to compute the Gibbs free energies at 298 K. The first () and second () oxidation potentials in V vs. Ag/Ag^+ were calculated using Eqs. 4 and 5 below:

(4)

(5)

where is the potential difference between the standard hydrogen electrode and the reference Ag/Ag^+ electrode (which is ≈ -4.78 V).[35] In these expressions, and are the differences between the Gibbs free energies of the singly (or doubly) oxidized and neutral solvated redoxmer molecules, respectively. The same DFT model was used to compute isotropic hyperfine coupling constants (hfcc's) in the gas phase radical cations.

Symmetric Flow Cell Tests. To obtain the 50% SOC electrolytes of MEEDPD, four H-type bulk electrolysis cells each containing 5.2 mL of 0.1 M or 0.5 M MEEDPD and 1 M LiTFSI/MeCN in the two chambers were charged at 8 mA (~0.57C) for 52 min in an argon-filled MBraun glove box with O_2 and water levels below 5 ppm. The total electrolytes in the four working chambers (20 mL) were removed, split equally and loaded in the two perfluoroalkoxyalkane reservoirs (Savillex) of the pre-assembled symmetric flow cell. The polypropylene flow cell included two 2.4 cm^2 carbon felt electrodes, a 175 μm thick Daramic® porous separator (Owensboro, KY), Teflon gaskets and Norprene tubing. The detailed architecture of the flow cell can be found in Ref. [36]. All flow cell components were dried overnight in vacuum at 80°C before use. These electrolytes were circulated at 20 mL min^{-1} using a Masterflex L/S peristaltic pump. To estimate the flow cell resistance, electrochemical impedance spectroscopy (EIS) was performed before and after the cycling tests using a Solartron SI 1287A electrochemical interface with SI 1250E frequency response analyzer. Before the galvanostatic cycling, a voltage-controlled rate test was performed with the current density increasing from 20 to 30 to 40 to 50 mA cm^{-2} in steps of 5 cycles. The long-term cycling was performed at 50 mA cm^{-2} with the voltage cutoff of ±0.75 V.

Symmetric H-Cell Test. The symmetric H-cell cycling test was performed in air using a borosilicate H-cell with the same design. The working and counter chambers each contained 4.0 mL of 2 mM redoxmer and 0.5 M LiTFSI in MeCN with vigorous stirring at 1,000 rpm. A porous ceramic disk (P5 frit, Adams and Chittenden) separated the two chambers. In each chamber, reticulated vitreous carbon (45 PPI, ERG Aerospace Corporation) was used as the electrode. An $Ag/AgNO_3$ quasi-reference electrode was placed as close as possible to the working electrode and was used to control the cell potential. The H-cell was fully charged galvanostatically at 5C (1.072 mA) and the electrolyte in the counter chamber was replaced with a fresh solution. Then the cycling was performed using a constant current, constant voltage operation method, i.e., at 5C until the set working electrode potential was reached (±0.1 V vs. Ag/Ag^+) followed by standing at the cutoff voltages until the current decreased below 0.1C.

Flow Full-Cell Tests. The flow full-cell test was performed using a different cell design that is capable of improved sealing with higher compression forces to reduce solvent evaporation. The parts included two SIGRACELL® graphite felt electrodes (GFD2.5, 2.5 mm thick, SGL Carbon, Germany) sandwiching a Daramic® porous separator (800 microns thick). The active area was 5 cm^2. Inside the glove box, mixed-reactant electrolytes (10 mL) containing 0.1 M BzNSN and 0.1 M MEEDPD in 1.0 M LiTFSI in MeCN were loaded to each of the two reservoirs and were circulated at 20 mL min^{-1}. The flow cell was tested at a constant current of 20 mA cm^{-2} with cutoff voltages at 1.2 ~ 2.0 V.

Acknowledgments

This work was partially supported by the Joint Center for Energy Storage Research (JCESR), an Energy Innovation Hub funded by the U.S. Department of Energy, Office of Science, Basic Energy Sciences. The authors also thank financial support from the U.S. National Science Foundation (Award No. CHE-2055222). The submitted manuscript has been created by UChicago Argonne, LLC, Operator of Argonne National Laboratory ("Argonne"). Argonne, a U.S. Department of Energy Office of Science laboratory, is operated under Contract No. DE-AC02-06CH11357. The U.S. Government retains for itself, and others acting on its behalf, a paid-up

References

(1) Soloveichik, G. L. Flow batteries: current status and trends. *Chemical reviews* **2015**, *115* (20), 11533-11558.
(2) Winsberg, J.; Hagemann, T.; Janoschka, T.; Hager, M. D.; Schubert, U. S. Redox-flow batteries: from metals to organic redox-active materials. *Angewandte Chemie International Edition* **2017**, *56* (3), 686-711.
(3) Li, M.; Rhodes, Z.; Cabrera-Pardo, J. R.; Minteer, S. D. Recent advancements in rational design of non-aqueous organic redox flow batteries. *Sustain Energ Fuels* **2020**, *4* (9), 4370-4389.
(4) Gong, K.; Fang, Q. R.; Gu, S.; Li, S. F. Y.; Yan, Y. S. Nonaqueous redox-flow batteries: organic solvents, supporting electrolytes, and redox pairs. *Energ Environ Sci* **2015**, *8* (12), 3515-3530. DOI: 10.1039/c5ee02341f.
(5) Wei, X. L.; Pan, W. X.; Duan, W. T.; Hollas, A.; Yang, Z.; Li, B.; Nie, Z. M.; Liu, J.; Reed, D.; Wang, W.; Sprenkle, V. Materials and Systems for Organic Redox Flow Batteries: Status and Challenges. *Acs Energy Lett* **2017**, *2* (9), 2187-2204. DOI: 10.1021/acsenergylett.7b00650.
(6) Ding, Y.; Zhang, C. K.; Zhang, L. Y.; Zhou, Y. E.; Yu, G. H. Molecular engineering of organic electroactive materials for redox flow batteries. *Chem Soc Rev* **2018**, *47* (1), 69-103. DOI: 10.1039/c7cs00569e.
(7) Luo, J. A.; Hu, B.; Hu, M. W.; Zhao, Y.; Liu, T. L. Status and Prospects of Organic Redox Flow Batteries toward Sustainable Energy Storage. *Acs Energy Lett* **2019**, *4* (9), 2220-2240. DOI: 10.1021/acsenergylett.9b01332.
(8) Wei, X. L.; Xu, W.; Huang, J. H.; Zhang, L.; Walter, E.; Lawrence , C.; Vijayakumar, M.; Henderson, W. A.; Liu, T. B.; Cosimbescu, L.; et al. Radical Compatibility with Nonaqueous Electrolytes and Its Impact on an All-Organic Redox Flow Battery. *Angew Chem Int Edit* **2015**, *54* (30), 8684-8687. DOI: 10.1002/anie.201501443.
(9) Zhang, J. J.; Slikrob, I. A.; Assary, R. S.; Tung, S. O.; Silcox, B.; Curtiss, L. A.; Thompson, L.; Zhang, L. Toward Improved Catholyte Materials for Redox Flow Batteries: What Controls Chemical Stability of Persistent Radical Cations? *J Phys Chem C* **2017**, *121* (42), 23347-23358. DOI: 10.1021/acs.jpcc.7b08281.
(10) Zhang, J. J.; Huang, J. H.; Robertson, L. A.; Assary, R. S.; Shkrob, I. A.; Zhang, L. Elucidating Factors Controlling Long-Term Stability of Radical Anions for Negative Charge Storage in Nonaqueous Redox Flow Batteries. *J Phys Chem C* **2018**, *122* (15), 8116-8127. DOI: 10.1021/acs.jpcc.8b01434.
(11) Armstrong, C. G.; Toghill, K. E. Stability of molecular radicals in organic non-aqueous redox flow batteries: A mini review. *Electrochem Commun* **2018**, *91*, 19-24. DOI: 10.1016/j.elecom.2018.04.017.
(12) Lai, Y. Y.; Li, X.; Zhu, Y. Polymeric Active Materials for Redox Flow Battery Application. *Acs Appl Polym Mater* **2020**, *2* (2), 113-128. DOI: 10.1021/acsapm.9b00864.
(13) Michaelis, L.; Schubert, M. P.; Granick, S. The Free Radicals of the Type of Wurster's Salts. *J Am Chem Soc* **1939**, *61* (8), 1981–1992. DOI: 10.1021/ja01877a013.
(14) Zhu, Y. G.; Du, Y.; Jia, C.; Zhou, M.; Fan, L.; Wang, X.; Wang, Q. Unleashing the power and energy of LiFePO4-based redox flow lithium battery with a bifunctional redox mediator. *Journal of the American Chemical Society* **2017**, *139* (18), 6286-6289.
(15) Chen, Y.; Gao, X.; Johnson, L. R.; Bruce, P. G. Kinetics of lithium peroxide oxidation by redox mediators and consequences for the lithium–oxygen cell. *Nature communications* **2018**, *9* (1), 1-6.
(16) Störle, C.; Eyer, P. Reactions of the Wurster's blue radical cation with thiols, and some properties of the reaction products. *Chemico-Biological Interactions* **1991**, *78* (3), 333-346. DOI: 10.1016/0009-2797(91)90063-D.

(17) Chaka, G.; Bakac, A. Two-electron oxidation of *N*,*N*,*N′*,*N′*-tetramethylphenylenediamine with a chromium(V) salen complex. *Dalton T* **2009**, (2), 318-321. DOI: 10.1039/b811140e.
(18) Pott, G. T.; Kommandeur, J. Magnetic Transition of Wurster's Bluo Perchlorate. I. The Low-Temperature Phase. *J Chem Phys* **1967**, *47* (2), 395-401. DOI: 10.1063/1.1711907.
(19) Stanic, P.; Niksic-Franjic, I.; Molcanov, K. Pancake-Bonded Dimers of Semiquinone Radical Cations of N,N,N′,N′-Tetramethyl-p-phenylenediamine (Wurster's Blue). *Cryst Growth Des* **2023**, *23* (6), 4571-4579. DOI: 10.1021/acs.cgd.3c00342.
(20) Grilj, J.; Laricheva, E. N.; Olivucci, M.; Vauthey, E. Fluorescence of Radical Ions in Liquid Solution: Wurster's Blue as a Case Study. *Angew Chem Int Edit* **2011**, *50* (19), 4496-4498. DOI: 10.1002/anie.201100015.
(21) Hausser, K. H.; Murrell, J. N. Pi Complexes between Organic Free Radicals. *J Chem Phys* **1957**, *27* (2), 500–504. DOI: 10.1063/1.1743757.
(22) Uemura, K.; Nakayama, S.; Seo, Y.; Suzuki, K.; Ooshika, Y. The Temperature Dependence of the Absorption Spectra of Wurster's Blue-type Ion Radicals. *B Chem Soc Jpn* **1966**, *39* (6). DOI: 10.1246/bcsj.39.1348.
(23) Kimura, K.; Yamada, H.; Tsubomura, H. Electronic Absorption Spectra of Dimers of *p*-Benzosemiquinone Anion and Wurster's Cations in Solution. *J Chem Phys* **1968**, *48* (1), 440–444. DOI: 10.1063/1.1667941.
(24) Huang, J. H.; Cheng, L.; Assary, R. S.; Wang, P. Q.; Xue, Z.; Burrell, A. K.; Curtiss, L. A.; Zhang, L. Liquid Catholyte Molecules for Nonaqueous Redox Flow Batteries. *Adv Energy Mater* **2015**, *5* (6), 1401782. DOI: 10.1002/Aenm.201401782.
(25) Compton, R. G.; Banks, C. E. *Understanding voltammetry*; World Scientific, 2018.
(26) Luo, J.; Sam, A.; Hu, B.; DeBruler, C.; Wei, X. L.; Wang, W.; Liu, T. L. Unraveling pH dependent cycling stability of ferricyanide/ferrocyanide in redox flow batteries. *Nano Energy* **2017**, *42*, 215-221. DOI: 10.1016/j.nanoen.2017.10.057.
(27) Goulet, M. A.; Aziz, M. J. Flow Battery Molecular Reactant Stability Determined by Symmetric Cell Cycling Methods. *J Electrochem Soc* **2018**, *165* (7), A1466-A1477. DOI: 10.1149/2.0891807jes.
(28) Milshtein, J. D.; Kaur, A. P.; Casselman, M. D.; Kowalski, J. A.; Modekrutti, S.; Zhang, P. L.; Attanayake, N. H.; Elliott, C. F.; Parkin, S. R.; Risko, C.; et al. High current density, long duration cycling of soluble organic active species for non-aqueous redox flow batteries. *Energ Environ Sci* **2016**, *9* (11), 3531-3543. DOI: 10.1039/c6ee02027e.
(29) Luo, Q. T.; Li, L. Y.; Wang, W.; Nie, Z. M.; Wei, X. L.; Li, B.; Chen, B. W.; Yang, Z. G.; Sprenkle, V. Capacity Decay and Remediation of Nafion-based All-Vanadium Redox Flow Batteries. *Chemsuschem* **2013**, *6* (2), 268-274. DOI: DOI 10.1002/cssc.201200730.
(30) Duan, W. T.; Huang, J. H.; Kowalski, J. A.; Shkrob, I. A.; Vijayakumar, M.; Walter, E.; Pan, B. F.; Yang, Z.; Milshtein, J. D.; Li, B.; et al. "Wine-Dark Sea" in an Organic Flow Battery: Storing Negative Charge in 2,1,3-Benzothiadiazole Radicals Leads to Improved Cyclability. *Acs Energy Lett* **2017**, *2* (5), 1156-1161. DOI: 10.1021/acsenergylett.7b00261.
(31) Zhang, J.; Huang, J.; Robertson, L. A.; Shkrob, I. A.; Zhang, L. Comparing calendar and cycle life stability of redox active organic molecules for nonaqueous redox flow batteries. *Journal of Power Sources* **2018**, *397*, 214-222.
(32) *Gaussian 16, revision C.01*; 2016. https://gaussian.com/citation/ (accessed.
(33) Cossi, M.; Rega, N.; Scalmani, G.; Barone, V. Energies, Structures, and Electronic Properties of Molecules in Solution with the C-PCM Solvation Model *J. Comput. Chem.* **2003**, *24*, 669-681.
(34) Barone, V.; Cossi, M. Quantum Calculation of Molecular Energies and Energy Gradients in Solution by a Conductor Solvent Model. *J. Phys. Chem. A* **1998**, *102*, 1995-2001.
(35) Assary, R. S.; Brushett, F. R.; Curtiss, L. A. Reduction potential predictions of some aromatic nitrogen-containing molecules. *RSC Adv.* **2014**, *4*, 57442-57451.
(36) Milshtein, J. D.; Barton, J. L.; Darling, R. M.; Brushett, F. R. 4-acetamido-2, 2, 6, 6-tetramethylpiperidine-1-oxyl as a model organic redox active compound for nonaqueous flow batteries. *Journal of Power Sources* **2016**, *327*, 151-159.

Figures and Tables

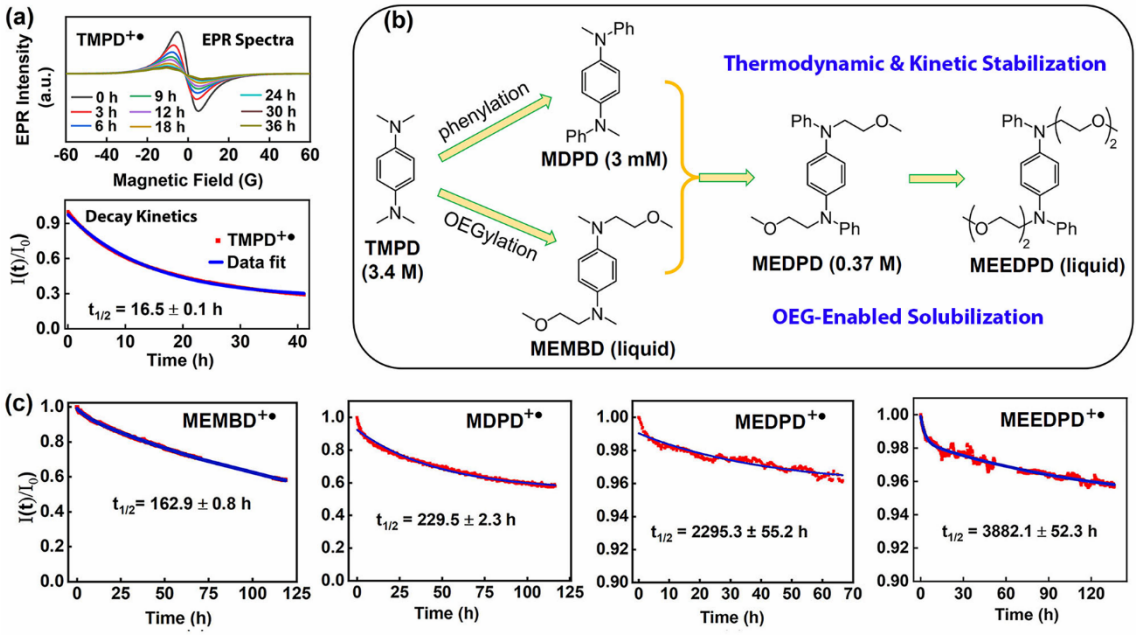

Figure 1. **(a)** Time-dependent EPR spectra (top) and fitted decay kinetics (bottom) of 50 mM $TMPD^{+\bullet}$; (b) illustration of the progressive molecular design approach; (c) The decay kinetics of 50 mM $MEMBD^{+\bullet}$, 2 mM $MDPD^{+\bullet}$, 50 mM $MEDPD^{+\bullet}$, and 50 mM $MEEDPD^{+\bullet}$. In these panels, the red circles are the experimental , and the blue lines are the least-squares exponential fits. The low concentration of $MDPD^{+\bullet}$ was used due to its low solubility in electrolyte. The supporting electrolyte was 0.5 M LiTFSI in MeCN.

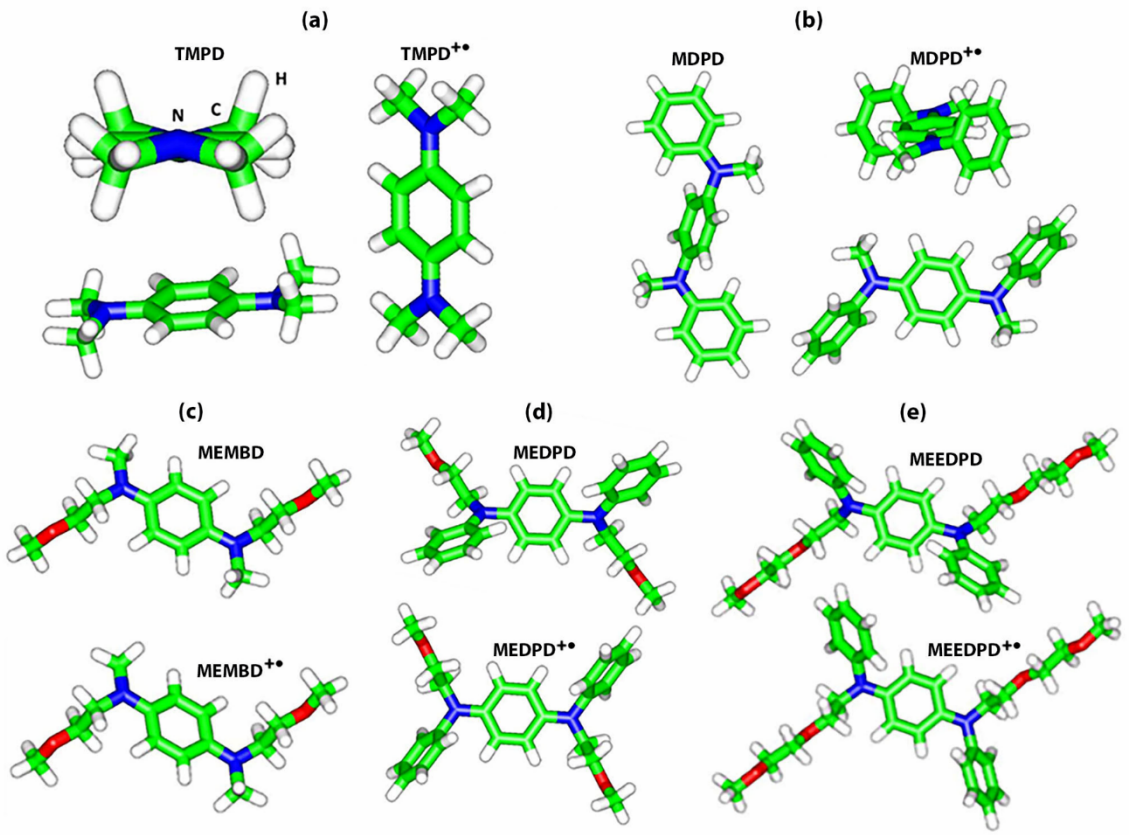

Figure 2. DFT calculations of gas-phase optimized structures for (a) TMPD, (b) MDPD, (c) MEMBD, (d) MEDPD, and (e) MEEDPD in the neutral and singly charged states.

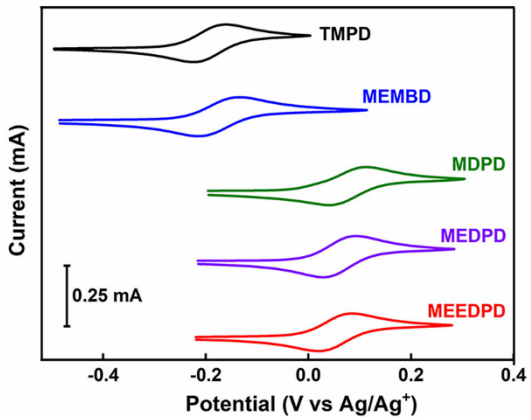

Figure 3. Cyclic voltammograms for 1e$^-$ oxidation of TMPD, MEMBD, MEDPD and MEEDPD at 5 mM and MDPD at 2 mM obtained with a sweep rate of 100 mV s^{-1}. The supporting electrolyte was 0.5 M LiTFSI in MeCN.

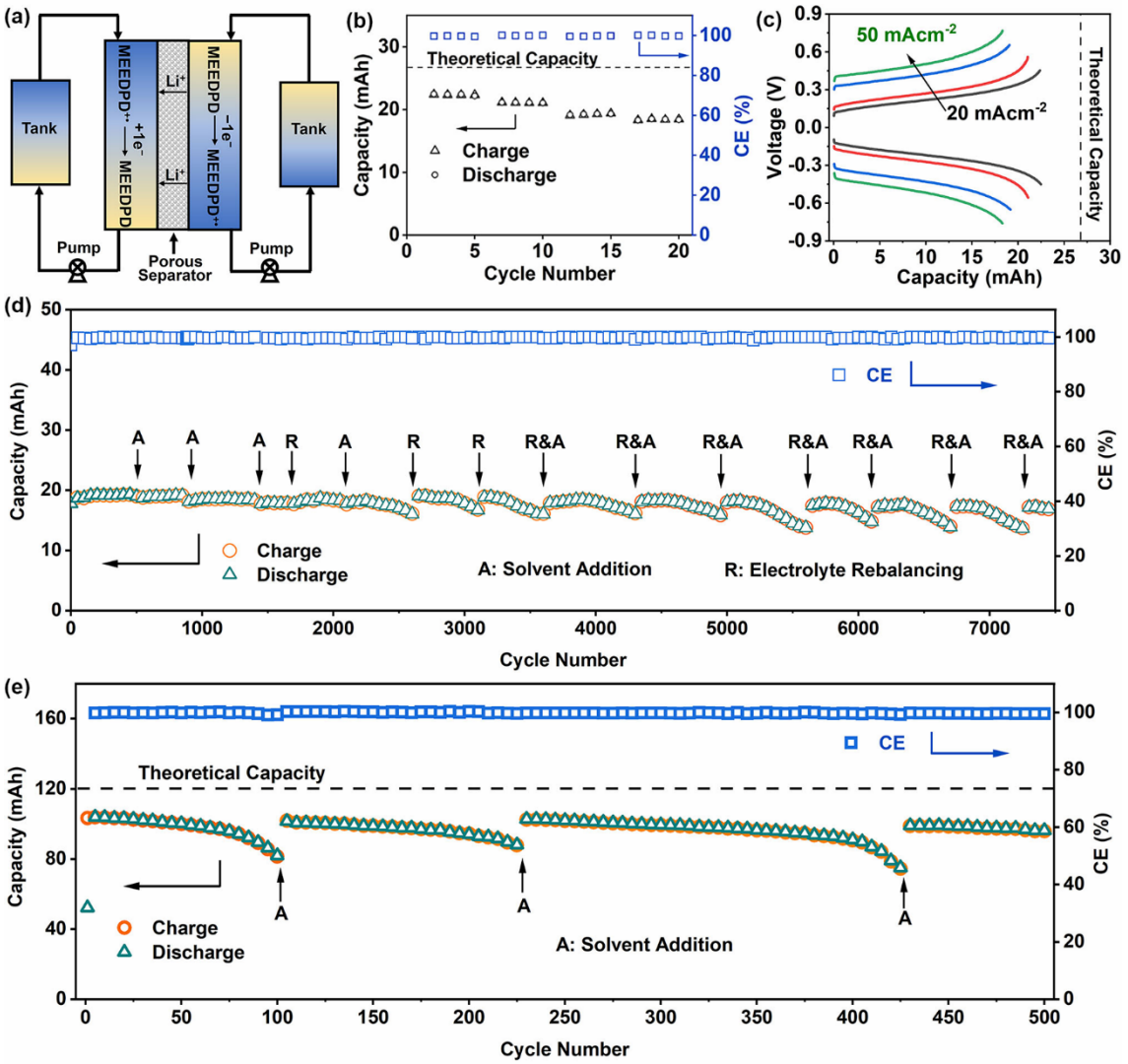

Figure 4. Symmetric MEEDPD flow cells: (a) Schematic illustration of a symmetric flow cell; (b) Charge and discharge capacities and (c) voltage curves of the 0.1 M symmetric flow cell at different current densities; (d) Long cycling of the 0.1 M symmetric flow cell at 50 mA cm^{-2}; (e) Long cycling of the 0.5 M symmetric flow cell at 50 mA cm^{-2}.